Controlling Gold Nanoparticles Aggregation in Continuous Flow Microreactor for Robust Production of Ultrasensitive NIR SERS Nanotags

Alexandre Verdin[1*], Pierre Stiernet[2], Louise Lejeune[3], Jean-Christophe M. Monbaliu[4,5], Sophie Hermans[3], Gauthier Eppe[1] and Cedric Malherbe[1].

[1] Mass Spectrometry Laboratory, MolSys Research Unit, University of Liège, 4000 Liège, Belgium.
[2] Center for Education and Research on Macromolecules (CERM), CESAM Research Unit, University of Liège, 4000 Liège, Belgium.
[3] Institute of Condensed Matter and Nanosciences (IMCN), UCLouvain, Place L. Pasteur 1, 1348 Louvain-la-Neuve, Belgium.
[4] Center for Integrated Technology and Organic Synthesis (CiTOS), MolSys Research Unit, University of Liège, 4000 Liège, Belgium.
[5] WEL Research Institute, Avenue Pasteur 6, 1300 Wavre, Belgium.

*Corresponding author: Alexandre Verdin – alexandre.verdin@uliege.be

Abstract

Surface-Enhanced Raman Scattering (SERS) nanotags are powerful tools for bio-analytical applications owing to their spectral specificity and detection sensitivity. Achieving strong SERS signals requires the generation of intense electromagnetic hot-spots, which are typically formed between closely spaced plasmonic nanoparticles, making the design of well-controlled nano-aggregates a promising approach for enhancing sensitivity in applications using SERS nanotags. This study demonstrates a flow chemistry approach for the controlled production of gold nano-aggregates optimized for Surface-Enhanced Raman Scattering (SERS) under near infrared (NIR) excitation. Using a two-stage microreactor system, 30 nm gold nanoparticles (Au NPs) are aggregated in a controlled manner with Malachite Green isothiocyanate (MGITC), acting simultaneously as Raman reporter and aggregating agent, then aggregation is rapidly quenched using HS-PEG-COOH or HS-PEG-Folic Acid (FA) to stabilise the nano-aggregates. Systematic variation of MGITC flow rate and reactor residence time enabled tunable aggregation, as confirmed via UV-Vis spectroscopy, Dynamic Light Scattering (DLS), Transmission Electron Microscopy (TEM) and SERS. The flow setup also offered high reversibility, with on-demand switching between aggregation states during the reactor operation. The best performing nano-aggregates provided over 100-fold SERS sensitivity improvement compared to non-aggregated Au NPs. Aggregation quenching with HS-PEG-FA offered additional targeting capabilities, enabling the complete production of nano-aggregates able to target cancer cells overexpressing folate receptors. In cancer tissue imaging experiments under 785 nm excitation, the nano-aggregates generated high-contrast SERS maps, while classical non-aggregated Au tags failed to generate detectable signals. Our platform offers on-demand production of tailored, ultrasensitive SERS tags suitable for biomedical imaging and diagnostics, combining enhanced signal strength and biological specificity.

Keywords

- Gold nanoparticles
- Microfluidic synthesis
- Controlled aggregation
- SERS
- Near Infrared

Introduction

Nanotags based on Surface-Enhanced Raman Scattering (SERS) have emerged as a promising tool for bio-analytical applications, ranging from lateral flow assays for detecting biomolecules in biological fluids to the detection of biomolecules directly in cells or tissues samples [1,2]. In recent years, efforts have been dedicated to improve the sensitivity of the nanotags, especially under excitation in the near infrared (NIR) region [3,4], due to the higher tissue penetration of light and reduced background autofluorescence at these wavelengths [5]. SERS nanotags optimised for NIR are therefore well-suited for *in vivo* imaging, point-of-care diagnostics, and other applications requiring measurements in biological samples [6–8].

Traditionally, spherical nanoparticles (gold or silver) are used to build the plasmonic core of SERS tags because of their wide availability, ease of synthesis and functionalisation, and well-understood behaviour in biological conditions [9]. However, these nanoparticles provide limited signal enhancement capabilities in NIR SERS due to the absence of localised surface plasmonic resonances (LSPR) in the NIR region. Two strategies have been proposed to improve the SERS performances of nanotags in the NIR region. First, nanoparticles with anisotropic shapes, such as rods, stars or cubes can be used as plasmonic core [9–12]. These nanostructures have tunable LSPR across the visible and NIR range of wavelengths, and also have the ability to concentrate the electric field around their tips and edges, similarly to an antenna, leading to larger enhancement factors than spherical NPs [9,13,14]. However, their synthesis is not as straightforward as the synthesis of spherical NPs, and they still suffer from long-term stability issues that ultimately hinders their applicability [10,15,16]. A second strategy is to integrate hot-spots directly in the nanostructures, for example by assembling spherical NPs in core-satellite structures [17] or by controlling the formation of multimers (or aggregates) of spherical NPs [18,19]. Such nanostructures usually exhibit new plasmonic resonances in the NIR region due to the coupling of plasmons of the different particles composing the structure [20]. Aggregates are highly interesting for use as SERS nanotags because the extent of aggregation can be varied to provide tunable optical properties starting from simple spherical NPs [19,21,22] However, accurately controlling the aggregation of colloidal NPs is a longstanding challenge in nanoscience [23], and especially for SERS applications where the extent of aggregation has a massive influence on the SERS signal [24].

Different strategies have been implemented to control the aggregation of noble metal nanoparticles toward the formation of SERS tags (Figure S1). A widely used approach consists in using specific chemicals (i), such as diamine molecules to direct the aggregation of single spherical Au NPs, followed by labelling with Raman reporter molecules and silica encapsulation [25]; structuring agents like cucurbit[7]uril to control the assembly of NPs, followed with thiol-poly(ethylene glycol) (HS-PEG) quenching to trap aggregates in defined states [26, 27]; or polymers like polyvinylpyrrolidone (PVP) acting as both aggregating agents and stabiliser for the controlled aggregation of labelled silver NPs [18]. Another

approach is to take advantage of hydrophobic interactions and solvent polarity (ii), allowing for example fine-tuning of aggregation through the balance of hydrophobic destabilisers and hydrophilic stabilisers [21]; or the co-solvent-induced aggregation of 4-mercaptobenzoic acid (4-MBA)-labelled Au NPs, followed by PEG stabilisation [28], and surface ligand concentration and solvent polarity can be leveraged to form well-defined aggregates [29]. Physical methods (iii) have also been investigated, such as flash freezing/thawing [30], [31], or centrifugation with an appropriate stabiliser at the surface of the NPs [32]. Nevertheless, all these described methods require several chemicals or the implementation of physical processes, and most of the time the incorporation of the Raman-reporter molecules is conducted afterwards.

An appealing approach is to use Raman reporter molecules, such as organic dyes, directly as aggregating agent enabling the straightforward formation of nano-aggregates without the need of additional chemicals required to trigger the aggregation. Moreover, by inducing the aggregation process, Raman-reporter molecules are directly trapped between the NPs and benefit from the strong electric field hot-spots leading to intense SERS signals [33],[34]. Several dyes commonly used as Raman-reporter molecules, such as malachite green isothiocyanate (MGITC), crystal violet (CV), and Nile Blue A (NBA), are well suited as aggregating agent because they are cationic, hydrophobic molecules that will strongly destabilise negatively-charged Au NPs [19]. However, controlling dye-induced aggregation is difficult due to the critical role of local dye-to-NP stoichiometry. As most colloidal chemistry studies have been conducted in batch processes using conventional glassware, mixing is typically suboptimal [35]. Upon addition, the dye molecules create local regions of high concentration that require time to disperse uniformly. Consequently, NPs near these high concentration regions are rapidly saturated due to the high affinity of dyes for metallic surfaces, leading to excessive aggregation. In contrast, NPs located in depleted regions remain mostly uncoated, producing uneven and poorly controlled aggregates [36].

Microfluidics, where chemical reactions are conducted in microreactors (*i.e.* continuous-flow reactors with internal dimensioning < 500 µm), has a huge potential for chemical processes limited by mass and heat transfer [35,37]. Reaction paths with submillimeter dimensioning, with optionally the assistance of high-performance static mixing elements, provides significantly improved mixing efficiencies compared to macroscopic batch environments, and thus an excellent control over the local stoichiometry between reactants. Additionally, heat transfer also greatly benefits from a higher surface to volume ratio, altogether contributing to homogenous process conditions for reacting chemicals. When it comes to control the aggregation of noble metal nanoparticles toward the formation of SERS tag, it is expected that such level of control on process parameters should lead to less dispersed populations in terms of aggregates sizes. Additionally, under continuous-flow conditions, aggregates are spatially isolated as they progress downstream, reducing their interaction with newly forming aggregates and therefore avoiding uncontrolled secondary growth often seen in macroscopic batch settings. Therefore, we believe that this novel approach could provide a distinctive control over the aggregation of spherical

gold NPs [38], opening the way toward the robust production of nano-aggregates with large SERS enhancement factors.

Herein, we demonstrated that a straightforward microfluidic-scale flow setup provides a powerful tool to precisely modulate the dye-induced aggregation of Au NPs. We leveraged the unique assets of microfluidics to control the stoichiometry of reaction between 30 nm Au NPs and MGITC-dye, used simultaneously as aggregating agent and Raman-reporter molecule. By modulating the MGITC flow rate and the overall residence time in a first microreactor module, we accurately tuned the aggregation state of the Au NPs. Once the desired level of aggregation was reached, the aggregation process was rapidly quenched downstream, in a second concatenated microreactor module, by injection of HS-PEG-COOH. Moreover, continuous operation ensured high reproducibility, robustness, and tuneability of the aggregates, with average diameters up to 175 nm. The resulting aggregates remained stable for days and the best one showed at least a two-order-of-magnitude increase in SERS sensitivity compared to non-aggregated Au NPs under 785 nm excitation. Finally, by substituting the quenching agent with HS-PEG-Folic Acid (FA), we achieved the one-step preparation of highly active NIR SERS nanotags targeting folate receptors for high-contrast SERS imaging of cancerous tissues overexpressing folate receptors. The production of targeted aggregates is of high importance because folate receptors, especially Folate Receptor α (FRα), represent a target of growing interest in cancer research due to its overexpression in many tumor types while exhibiting a low expression in healthy tissue, enabling selective cancer targeting [39].

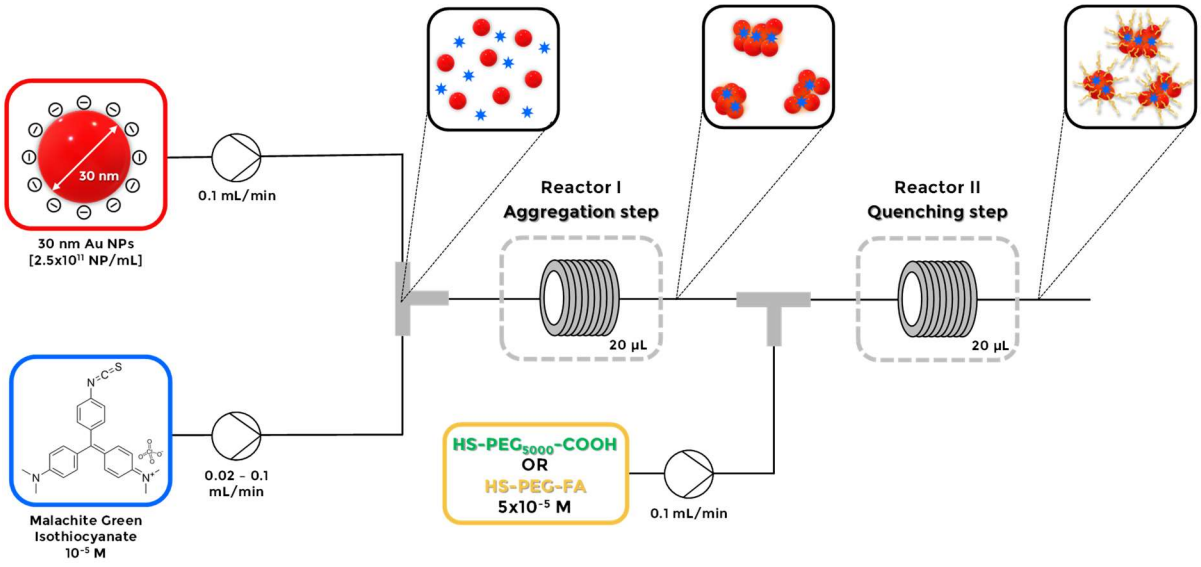

Figure 1. Schematic of the microfluidic setup used in this work to control the aggregation state of gold nanoparticles.

Materials and methods

Chemicals

Citrate-coated 30 nm gold nanoparticles were provided by NanoQ ® (Belgium) at a concentration of $2.5x10^{11}$ NP/mL (Optical Density = 4 at 529 nm). Malachite green isothiocyanate was purchased from ThermoFisher (M689). Poly (ethylene glycol) 2-mercaptoethyl ether acetic acid (HS-PEG-COOH, 5 kDa) was purchased from Merck (757845) and thiol-poly (ethylene glycol)-folic acid (HS-PEG-FA, 5 kDa) was purchased from Abbexa (abx085157).

Microfluidic setup

The continuous microfluidic reactors were assembled with high purity PFA tubing (1/16″ o.d., 0.01″ i.d., Achrom). Gold nanoparticles, MGITC and HS-PEG-COOH/FA solutions were pumped with high force syringe pumps (Chemyx Nexus 3000 or 6000), mixed through a T-static mixer and reacted in a PFA microreactor coil (40 cm of PFA tubing; 20 µL internal volume, reactor 1 - aggregation step). The first reactor was concatenated with a second microfluidic reactor module (reactor 2 – quenching step). The effluent from the first microfluidic reactor was mixed with a solution of HS-PEG-COOH/FA solution through another T-mixer, and reacted in the second PFA microreactor coil (40 cm of PFA tubing; 20 µL internal volume). The overall reaction effluents were then collected for characterisation. The entire system was operated at room temperature. A picture of the whole system can be found in Figure S2. Rates and concentration of the different solutions are summarised in Table S1.

Characterisation of the nano-aggregates

UV-Visible spectra of the produced nano-aggregates were obtained with an Uvikon XS (Secomam) spectrometer. Solutions were placed in PMMA cuvettes (1 cm) and spectra were collected from 330 to 1000 nm with a scan rate of 200 nm/min. SERS measurements were performed on a Horiba Labram 300 spectrometer. Solutions were placed in PMMA cuvettes (1 cm), and measurements were performed with a 20x magnification objective (NA = 0.4), 785 nm excitation (Cobolt 08-NLD), 85 mW of laser power at the sample, and 4 accumulations of 10 s signal acquisition. In all cases, spectra were collected from 840 to 1740 cm^{-1} with a grating of 1200/mm. Dynamic Light Scattering measurements were performed on a Malvern Delsa Nano instrument. Solutions were placed in PMMA cuvettes (1 cm), measurements were performed at 25°C and scattered light was collected at an angle of 135°. Intensity distributions were extracted for further analysis. Scanning Electron Microscopy (SEM) micrographs were obtained using a Tescan Clara instrument operating at an accelerating voltage of 15 kV. The aggregates were centrifuged to remove the HS-PEG-COOH excess, resuspended in tridistilled water and diluted by a factor 20 compared to their initial concentration. Then, 1 µL drops of aggregates solution were placed on an ITO-coated glass slide (Bruker) heated at 80°C to allow fast drying without significant coffee ring effect. Transmission Electron Microscopy (TEM) micrographs were obtained

using a Thermo Fisher TALOS F200i instrument operating at an accelerating voltage of 200 kV. A drop of the nano-aggregates solution (undiluted) was deposited on a TEM grid (FCF200-CU-50, Electron Microscopy Sciences) and left to dry before observation.

Data processing

UV-Visible spectra were normalised using the extinction value at 400 nm (interband transition of gold) since the amount of gold at the outlet of the reactor was stable (Figure S3). No other processing was applied to the UV-Vis spectra. Dynamic light scattering data were plotted as intensity (percent) as a function of the hydrodynamic diameter (log scale). TEM and SEM images were analysed using ImageJ software. Briefly, the diameter of the different aggregates or nanoparticles were measured using the length measurement tool, and the lengths in pixels scale were converted in metric scale (nm). SERS spectra were baseline-corrected using a 4^{th} order polynomial fit (Savitsky-Golay algorithm). The apex of the 1170 cm^{-1} band was used for intensity comparison for the measurements in solution.

Tissue preparation for mapping experiments

Formalin-Fixed Paraffin-Embedded (FFPE) ovarian cancerous tissues were provided by the university hospital Biobank (ULiège, Belgium). FFPE tissues were sectioned at 5 µm of thickness and deposited on SuperFrost Ultra+ glass slides. Tissues slides were heated 1 h at 60°C and immersed in 3 successive xylene baths for 2 min each, then 2 min in 80% ethanol, 2 min in 60% ethanol and finally 2 min in distilled water. Immediately after deparaffinization, tissues were placed in a slide holder containing target retrieval solution (Tris/EDTA buffer, pH 9, Dako). The slide holder was placed in a water bath and heated at 96°C for 15 min. After heating, samples were let to cool down to RT and were washed with phosphate buffer saline (PBS). Then, 500 µL of PBS with 2% Bovine Serum Albumin (BSA) were deposited on the slides and incubated 20 min at RT. The slides were rinsed with PBS and incubated for 2 h at RT with 250 µL of nanoparticles (either nano-aggregates or non-aggregated Au NPs, both at 11.3 µg Au/mL) suspended in PBS with 1% BSA. Finally, the slides were rinsed three times with PBS, once with distilled water and left to dry prior to the SERS analysis. Mapping experiments were performed with a 100x magnification objective (NA = 0.9) using an automated x-y table (Märzhäuser) and a spatial resolution of 1 µm in both directions. Spectra were acquired with 8.5 mW of laser power at the sample, and with a single acquisition of 1 s. SERS images were reconstructed by highlighting pixels with intensity at 1170 cm^{-1} above a defined threshold. The threshold was obtained by measuring the mean intensity and standard deviation at the position of the main band of MGITC (1170 cm^{-1}) in several spectra of the maps where no signal of MGITC was observed. The threshold was defined as: threshold = mean + 3*SD. All pixels satisfying this criterion were highlighted as a green pixel on the SERS maps.

Results and discussion

1. Control of the aggregation state under continuous microfluidic conditions

The experimental setup is composed of two microfluidic modules fluidically connected in series. The first microreactor (20 µL of internal volume) allows the mixing between the 30 nm Au NPs colloid and the MGITC solution (Figure 1). MGITC serves a dual purpose. Firstly, MGITC acts as aggregating agent, leading to the formation of nano-aggregates, bearing hot-spots that are highly effective for SERS under NIR excitation. Indeed, due to its strong affinity for gold and its cationic nature, adsorption of MGITC on citrate-stabilised Au NPs lowers the surface charges of the NPs and promote their aggregation. Moreover, its hydrophobic nature contributes to the aggregation process [21]. Secondly, MGITC serves as Raman-reporter because the molecules, which already have an intrinsically large Raman scattering cross section [19], will be trapped in the hot-spots inside the nano-aggregates, giving rise to very large SERS signals. In the second microreactor (20 µL internal volume), HS-PEG-COOH is injected in a large excess to swiftly quench the aggregation of the nano-aggregates produced upstream and stabilize them in their aggregation state, thereby preventing further evolution (Figure 1). The large excess of HS-PEG-COOH enables rapid binding of the PEG chains to the aggregates through thiol-gold interactions [40], preventing additional NPs to accumulate on the pre-existing aggregates thanks to strong steric hindrance and negative charge repulsion. This kind of strategy has already been implemented by other researchers and the ability of PEG to quench the aggregation has been demonstrated [26–28].

While keeping the flow rate of Au NPs constant at 0.1 mL/min, the flow rate of MGITC was varied from 0.02 to 0.1 mL/min to modulate the stoichiometry between Au NPs and aggregating agent. Residence time inside the first reactor varied from 10 to 6 seconds (Table S1). Note that such short aggregation times would be hardly achievable in batch process. For all conditions in the first reactor, the rate of HS-PEG-COOH was kept at 0.1 mL/min in the second reactor to insure efficient quenching (Figure S4) of all produced aggregates (residence time was 4 to 6 s). Figure 2A displays the UV-Vis spectra of the different solutions collected at the outlet of the setup. While the starting Au NPs of 30 nm exhibited a plasmonic band at 535 nm in the presence of PEG, an additional band appeared at longer wavelength upon aggregation (Figure 2A). Aggregates exhibit this red-shifted extinction band due to their larger sizes and the coupling of plasmonic mode of the individuals NPs [20]. By gradually increasing the MGITC flow rate, and thus the MGITC/Au NP ratio, a more extensive aggregation was promoted, as evidenced by the increase of extinction in the 600-1000 nm region. The position of the aggregate-related extinction band shifted from 682 nm (0.035 mL/min) to 725 nm (0.1 mL/min), indicating the gradual size increase of the aggregates.

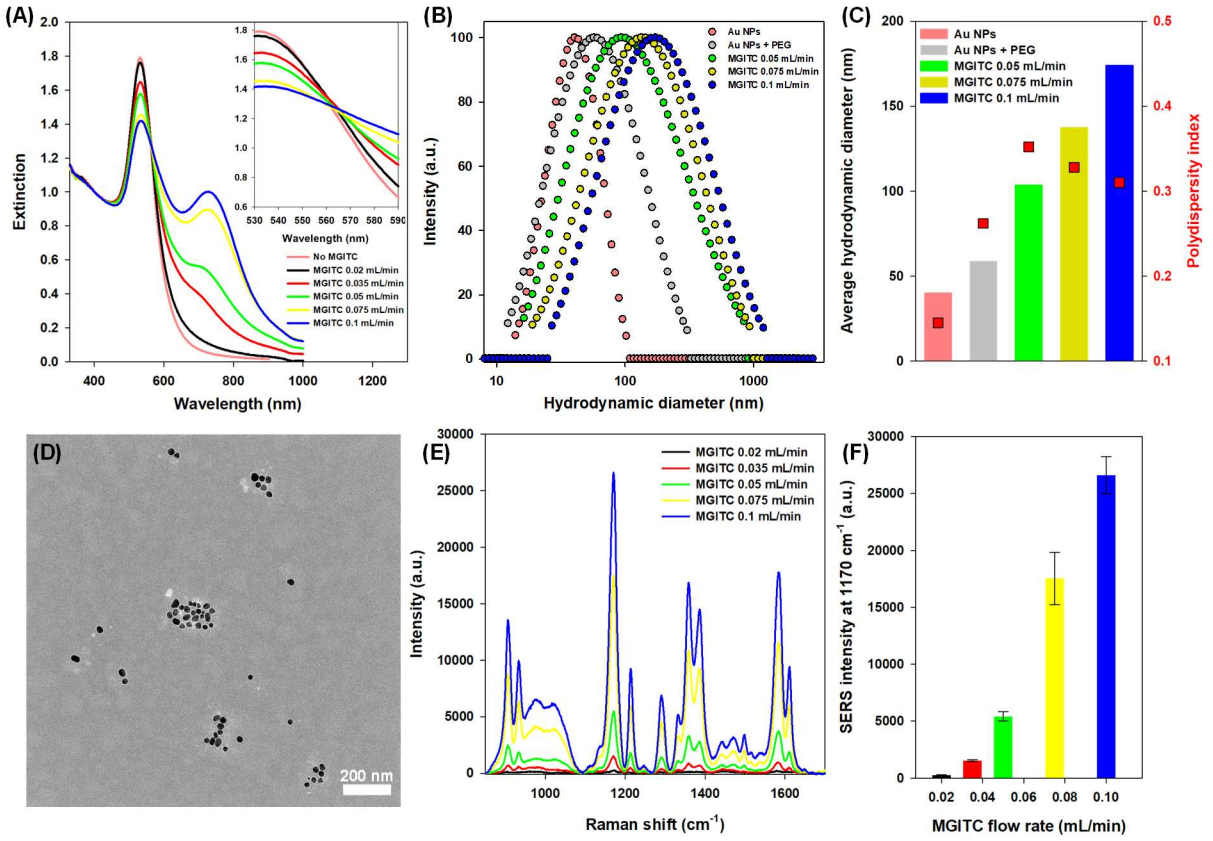

Figure 2. (A) UV-Vis extinction spectra of the nano-aggregates produced at increasing rates of MGITC. Insert highlights the presence of an isosbestic point at 565 nm. (B) Hydrodynamic diameter intensity distribution, obtained with DLS, of the starting Au NPs and of nano-aggregates samples produced under the largest MGITC rates. (C) Average hydrodynamic diameter and polydispersity index of the starting Au NPs and of nano-aggregates samples produced under the largest MGITC rates, illustrating the progressive increase of the average diameter. (D) Representative TEM image of the nano-aggregates produced under 0.1 mL/min MGITC rate (36k magnification). Scale bar is 200 nm. (E) Average SERS spectra (n = 3) obtained for the different nano-aggregates under 785 nm irradiation. (F) Intensity of the main band of MGITC at 1170 cm^{-1} for the different nano-aggregates produced under increasing MGITC rate. Error bars represent the standard deviation between three replicates.

Dynamic light scattering measurements showed an increase in the average hydrodynamic diameter of the nanoparticle population (Figure 2B) as the MGITC rate increased, confirming the formation of larger aggregates. For flow rates of MGITC ranging from 0.05 mL/min to 0.1 mL/min, the average hydrodynamic diameter increased from 94 to 173 nm (Figure 2C), with the whole population shifting toward higher diameter (Figure 2B). Moreover, size filtration experiments also confirmed the progressive shift toward larger sizes (Figure S5). Interestingly, UV-Vis spectra recorded as a function of MGITC flow rate presented an isosbestic point at 565 nm (Figure 2A, insert). The isosbestic point indicates that there is a clear inter-species transition from an initial state (isolated and non-aggregated population of single Au NPs) to another state corresponding to the aggregates [41–44]. When the flow rate of MGITC increases, there is a gradual increase of the proportion of aggregates compared to isolated Au NPs. The isosbestic point is a strong evidence that the use of microreactor allows to finely tune the extent of aggregation. Also, the isosbestic point indicates that the total concentration of optically active

species remains constant in the system, confirming that the total amount of gold in the system is conserved upon aggregation.

When aggregation was induced in batch with the same range of MGITC/Au NPs ratio, UV-Vis spectra of the corresponding aggregates did not present an isosbestic point (Figures S6 & S7). Moreover, the second extinction band was much larger, indicating the formation of a more dispersed population of aggregates in the conditions where the strongest aggregation was triggered (Figure S7). This highlights that aggregation was poorly controlled, and the absence of isosbestic point suggests that a part of the largest aggregates had already sedimented during the period between aggregation quenching and UV - Vis measurements. Also, increasing the MGITC/Au NPs ratio in batch did not necessarily led to a gradual increase of aggregation like we observed in flow, indicating that the aggregation process is less controled and possibly different between the two technologies (Figure S7). This phenomenon in batch was also reported recently with crystal violet as Raman reporter [45]. Additionally, when we performed three aggregation experiments in batch with the same MGITC/Au NPs ratio, we obtained aggregates with different optical properties, different average sizes and larger size dispersity, demonstrating again that the lack of control leads to unreproducible aggregates formation (Figure S8). Introducing a degree of automation through the use of microreactor could therefore reduce variability induced by human manipulation and provide a more robust approach for aggregates formation [46].

TEM images of the aggregates produced with a MGITC rate of 0.1 mL/min show that the aggregates are composed of closely-packed assemblies of several NPs (Figure 2D), forming mostly compact assemblies rather than chain-like structures [47]. SEM images were also obtained and provided similar observations (Figure S9). The nanogaps located at the junctions between NPs, where electric field hot-spots essential for SERS are generated, are clearly visible on the high resolution TEM images (Figure S10). Size analysis of 270 aggregates across several TEM images indicates that the average size of the main type of aggregates is 120 ± 80 nm (Figure S11). The diameter measured in TEM is smaller than the hydrodynamic diameter measured in DLS because TEM measures the physical diameter of the aggregates in dry state, while the hydrodynamic diameter is influenced by the presence of long PEG chains on the surface of the aggregates contributing to a larger hydration sphere [48]. Also, aggregates do not have a spherical shape, which influences the measured hydrodynamic diameter [49]. Aggregates are generally composed of 4 - 10 individual NPs with also few dimers observed, and the Au NPs composing the aggregates have a diameter of 31 ± 4 nm as expected. Moreover, only a few isolated NPs could be observed, indicating that a flow rate of 0.1 mL/min of MGITC induces almost complete aggregation of the whole Au NPs population, as also observed from the UV-Vis data (Figure S12). MGITC flow rates above 0.1 mL/min led to a lesser extent of aggregation due to the reduced residence time before quenching (Figure S13).

Regarding the SERS properties of the nano-aggregates produced in flow, we observed that the intensity of the SERS signal of MGITC increased significantly for larger aggregates (Figure 2E). Since higher MGITC flow rates increase the extent of the aggregation process, more aggregates and of larger size are produced with build-in hot-spots that result in a strong increase of the SERS signal of MGITC. Moreover, the evolution of the extinction at 725 nm and the intensity of the MGITC SERS signal displayed similar evolution with the increase of MGITC flow rate (Figure S14), indicating that the progressive formation of larger amounts of nano-aggregates caused the increase of SERS signal. The intensity of the main band of MGITC at 1170 cm^{-1} (C-H in plane stretching) increased by two orders of magnitude when the MGITC flow rate increased from 0.02 to 0.1 mL/min (Figure 2F). Also, the presence of different sizes of aggregates within the same production probably influences the SERS intensity, with a certain size fraction most likely dominating the overall signal [50]. This effect is especially present in samples produced under lower MGITC flow rates, exhibiting lower aggregation extent. We plan to further study this aspect in future work. Additionally, we performed fluorescence assays after Au dissolution to evaluate the amount of dye effectively trapped in the aggregates produced under varying dye flow rate. We observed that the amount of trapped dye increased only ≈ 3-fold when the dye rate increased from 0.02 to 0.1 mL/min, demonstrating that the huge signal increase (100-fold) obtained at the highest flow rate was indeed caused mainly by the formation of aggregates. Details can be found in the Supplementary Information (section 14, Figures S15 & S16). Finally, as expected, the SERS intensity did not decrease significantly after centrifugation of the aggregates to remove the PEG and eventual MGITC excess, demonstrating that MGITC molecules contributing to the signal are trapped in the nano-aggregates and no classical Raman signal from free MGITC molecules contributed to the overall detected signal (Figure S17).

In the microfluidic setup, the residence time in the first reactor is a key parameter to control the extent of aggregation. Indeed, when the residence time was halved by using a reactor with an internal volume of 10 µL instead of 20 µL but keeping the same flow rates of dye, smaller extent of aggregation was observed (Figure S18). These aggregates also showed weaker SERS signal (Crystal violet used as Raman-reporter), which is consistent with their lesser extent of aggregation (Figure S19). These results indicate that there is an evolution of the aggregation state during the flow through the first reactor (reactor 1 - aggregation step), and varying residence time can be used to control the extent of aggregation before the quenching step to modulate on-demand the optical properties of the aggregates. Also, the use of crystal violet for these experiments showed that the controlled aggregation strategy could be implemented with other Raman-reporter molecules, as also demonstrated for Rhodamine B isothiocyanate (RITC) (Figure S20).

Finally, off-line UV-Vis measurements allowed us to monitor the total amount of gold exiting the reactor in the different aggregation conditions by measuring the extinction at 400 nm (inter-band transition of gold, insensitive to the size and shape of the nanoparticles [51]) to evaluate the stability of

our system. In all cases, the amount of gold was stable (CV = 6.5 %, Figure S3), indicating that there was no significant clogging of the reactor due to the formation of aggregates, probably because the overall size of the aggregates was kept relatively small. We also observed that the nano-aggregates could be stored for at least two days without significant changes in their optical and SERS properties (Figure S21).

2. Reversibility of aggregates production in flow

One of the key aspects of continuous flow reactors is that reaction operating conditions can be tuned in real time to produce nano-aggregates with "on-demand" level of aggregation. To demonstrate the high control that our system allows, we started the experiment with a MGITC flow rate of 0.1 mL/min (i), producing a large degree of aggregation as discussed in section 1. After a few minutes of operation, the MGITC flow rate was then reduced to 0.02 mL/min (ii), producing markedly lower level of aggregation. Then we switched back to 0.1 mL/min (iii), then again to 0.02 mL/min (iv), and finally we returned to the initial rate of 0.1 mL/min (v). Au NPs flow rate was kept constant at 0.1 mL/min in all conditions. For every step, the properties of the produced aggregates were monitored with UV-visible spectroscopy, SERS and dynamic light scattering.

Figure 3 shows that the aggregates produced with a flow rate of dye of 0.1 mL/min had larger extent of aggregation evidenced by a strong extinction of the plasmonic band at 725 nm and an average hydrodynamic diameter of about 170 nm (Figure 3A and D). The same population of aggregates was repeatedly produced at steps (i), (iii) and (v) and they exhibited similar SERS signal enhancement (Figure 3B). When the system was switched to lower MGITC flow rate (0.02 mL/min) in steps (ii) and (iv), the level of aggregation decreased accordingly as evidenced by the absence of a second plasmonic band in the UV-Vis spectrum and a reduced SERS signal (Figure 3A and B). These results are consistent with the data described above in section 1. The robustness, reversibility and high level of control brought by microfluidics is illustrated in Figure 4C that summarizes these results by plotting the ratio of extinction at 725 and 535 nm (indicative of the level of aggregation, Figure 3C - left axis) and of the SERS intensity of the main band of MGITC (Figure 3C – right axis) for each step of the experiment. Each time the MGITC flow rate was changed, aggregates with properties similar to those from the previous corresponding step(s) were obtained.

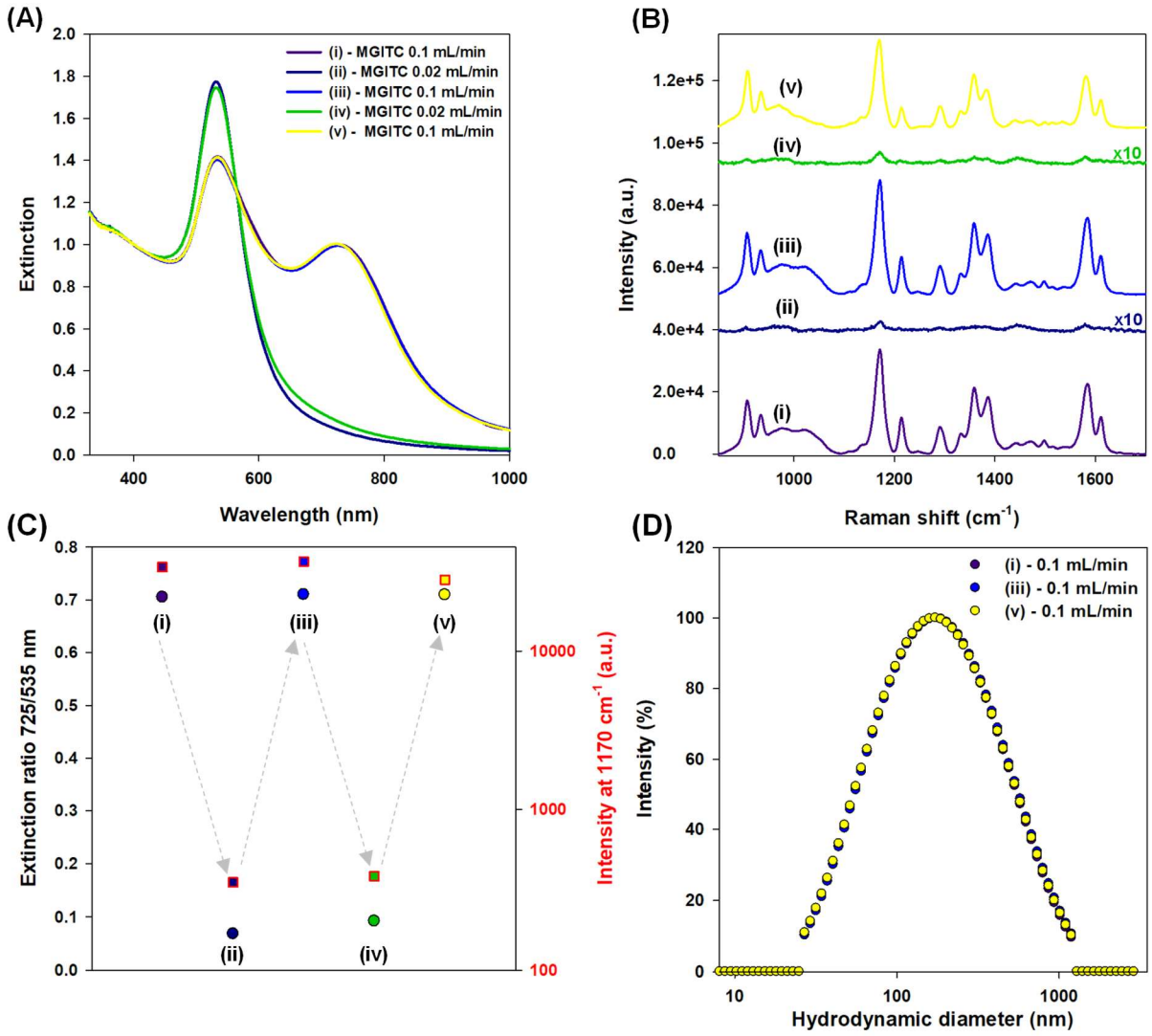

Figure 3. (A) UV-Visible and (B) SERS spectra of the aggregates obtained during the different steps of the reversibility experiment. SERS spectra for steps (ii) and (iv) were multiplied by a factor 10 for clarity. (C) Ratio between the extinction at 725 and 535 nm (left axis, circles), and SERS intensity of the 1170 cm^{-1} band of MGITC (right axis, squares) for the different steps of the reversibility experiment. (D) DLS intensity plot of the aggregates obtained during steps (i), (iii) and (v) of the reversibility experiment.

3. Targeted nanotags production using HS-PEG-FA as quenching agent

HS-PEG-COOH proved highly effective in stabilizing the produced nano-aggregates at a defined level of aggregation (as demonstrated in previous sections) and allowing their storage for a few days (Figures S21 & S22). However, it lacks specificity at targeting biological samples. Therefore, we substituted HS-PEG-COOH with chains terminated by folic acid (HS-PEG-FA) to combine the quenching efficiency of thiol-functionalized PEG with the targeting capability provided by folic acid. As previously demonstrated [52], [39], HS-PEG-FA-functionalized nanomaterials are able to selectively bind to folate receptors, which are overexpressed at the surface of several types of cancerous cells. As shown in Figure 4, when using HS-PEG-FA, nano-aggregates with similar optical properties than those quenched by HS-PEG-COOH were produced. Again, we finely and reversibly tuned the level of aggregation.

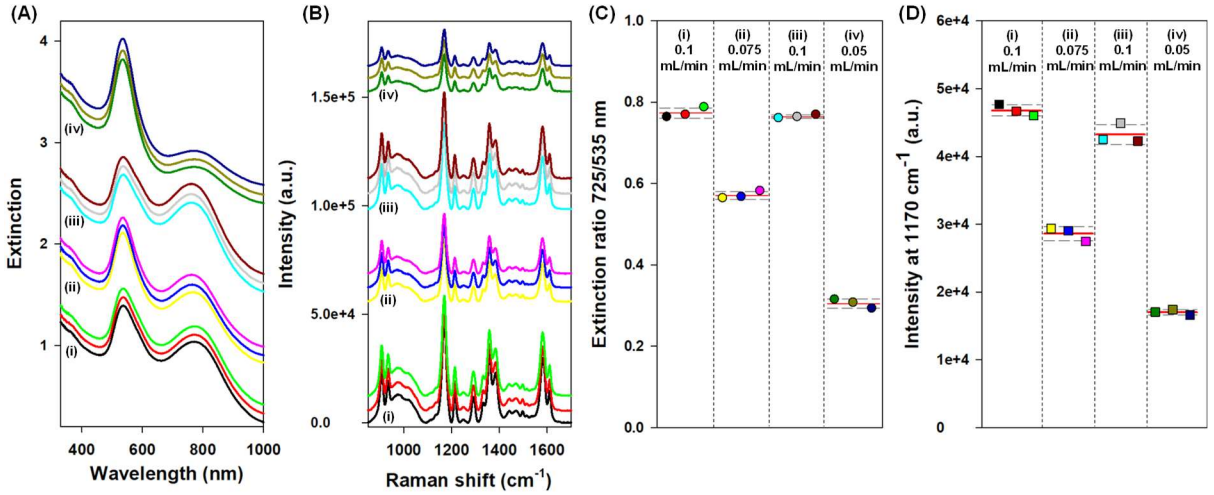

Figure 4. (A) UV-Vis spectra and (B) SERS spectra obtained during the runs at different MGITC flow rates followed by HS-PEG-FA quenching. For each MGITC flow rate, three spectra corresponding to three successive collected fractions are overlaid to demonstrate the stability of aggregates production when the MGITC flow rate is fixed. (C) Ratio between the extinction at 725 and 535 nm and (D) intensity of the main band of MGITC at 1170 cm^{-1} during the runs at different MGITC flow rates. Runs where performed at an MGITC flow rate of 0.1 mL/min (i), 0.075 mL/min (ii), 0.1 mL/min (iii) and 0.05 mL/min (iv). Plain red and dashed grey lines represent the average and standard deviation, respectively, from the three replicates.

Overall, the HS-PEG-FA afforded the same level of aggregation control than HS-PEG-COOH, and the nano-aggregates produced with this polymer quencher are similar to those produced in the previous sections. All in all, this concatenated microfluidic protocol enabled the production of functional nano-aggregates, with on demand control of their optical properties. Notably, these functional nano-aggregates displayed very high SERS sensitivity, and targeting capabilities toward folate receptors.

4. Increased SERS sensitivity – solution experiments

These nano-aggregates are very promising for bio-analytical applications due to the high level of control upon their aggregation level and because they can be readily excited under NIR irradiation (785 nm). We compared the sensitivity of our nano-aggregates (cond.: 0.1 mL/min MGITC flow rate) to non-aggregated Au nanoparticles for identical gold concentration. The 30 nm spherical Au NPs were functionalized with MGITC in conditions that avoid any significant aggregation (final concentration of MGITC in contact with the NPs = $4x10^{-7}$ M). They were then saturated with HS-PEG-FA to match the surface coating of nano-aggregates. These non-aggregated NPs are denoted "classical nanotags".

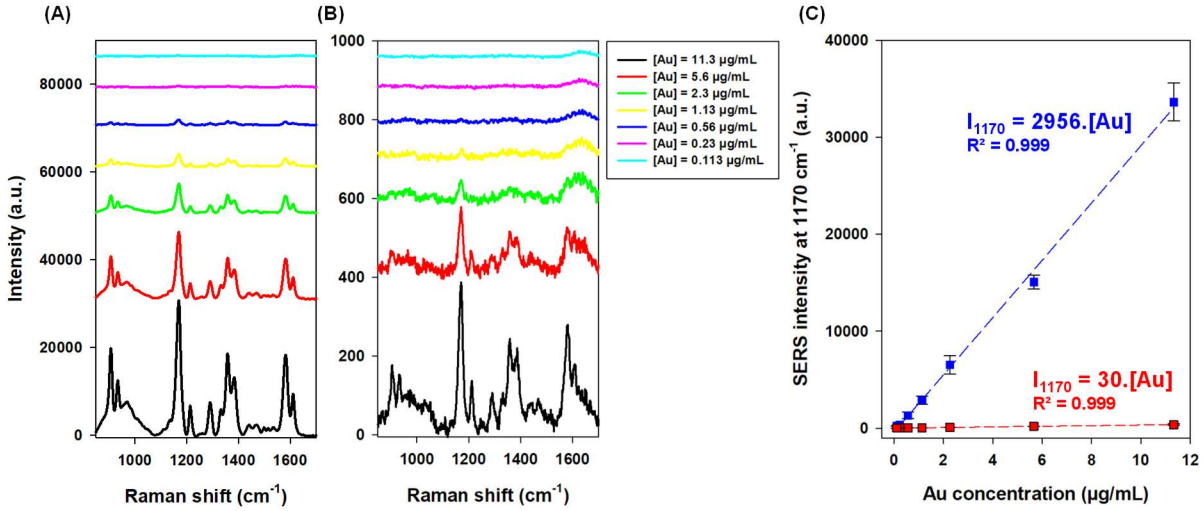

Figure 5. Average SERS spectra (n = 3) as a function of the Au concentration (µg/mL) for (A) the nano-aggregates produced with the microfluidic setup at 0.1 mL/min MGITC flow rate and (B) for the classical, non-aggregated Au nanotags. (C) Plots of the intensity of MGITC main band at 1170 cm^{-1} for the nano-aggregates (blue) and for the classical, non-aggregated Au nanotags (red) as a function of the Au concentration (µg/mL). Error bars represent the standard deviation between three replicates. Representative SERS spectra obtained for replicates at several concentration levels can be found in Figure S23. Zoom on the low intensity region can be found in Figure S24 to better observe the response of non-aggregated Au NPs.

Figures 5A and 5B show the SERS spectra obtained under 785 nm excitation for both systems as a function of the total gold concentration. Sensitivity was compared at equal total gold concentration (µg/mL) and not number of particles in solution as aggregation reduces the number of particles in solution. As can be observed, nano-aggregates produce much higher SERS signals than non-aggregated NPs because of the high density of hot-spots that are efficiently excited under 785 nm irradiation. Figure 5C shows the intensity of MGITC main band at 1170 cm^{-1} as a function of the total gold concentration for both systems. In both cases, the SERS signal intensity increases linearly with increasing gold concentration. Linear regressions were calculated for both systems and the ratio of the slopes was used to measure the gain of sensitivity provided by the nano-aggregates. A ratio of slope of ≈ 100 was obtained, indicating that the gold nano-aggregates provide at least a two order of magnitude gain in sensitivity in average compared to classical gold NPs when similar amount of gold is considered. If sensitivity was compared in conditions where the number of nano-objects is similar, it is expected that

the sensitivity gain provided by the nano-aggregates would be much higher as we estimated that in average the aggregates contained 4 - 10 NPs.

5. Tissue imaging at 785 nm with HS-PEG-FA quenched nano-aggregates

Nano-aggregates quenched with HS-PEG-FA and producing the largest SERS signal under 785 nm excitation (MGITC flow rate of 0.1 mL/min) were incubated (t = 2 hours) on cancerous ovarian tissue slide, which was subsequently washed to remove unbound nano-aggregates. An adjacent tissue slide was incubated with classical Au nanotags (non-aggregated 30 nm Au NPs functionalized with MGITC and HS-PEG-FA). The gold concentration of nano-aggregates and classical nanotags were equivalent (11.3 µg Au/mL) during the incubation with the tissues. We used a subtype of ovarian cancer known for highly overexpressing folate receptors (epithelial cancer), also as similar ovarian tissues were already analyzed in our previous work [53].

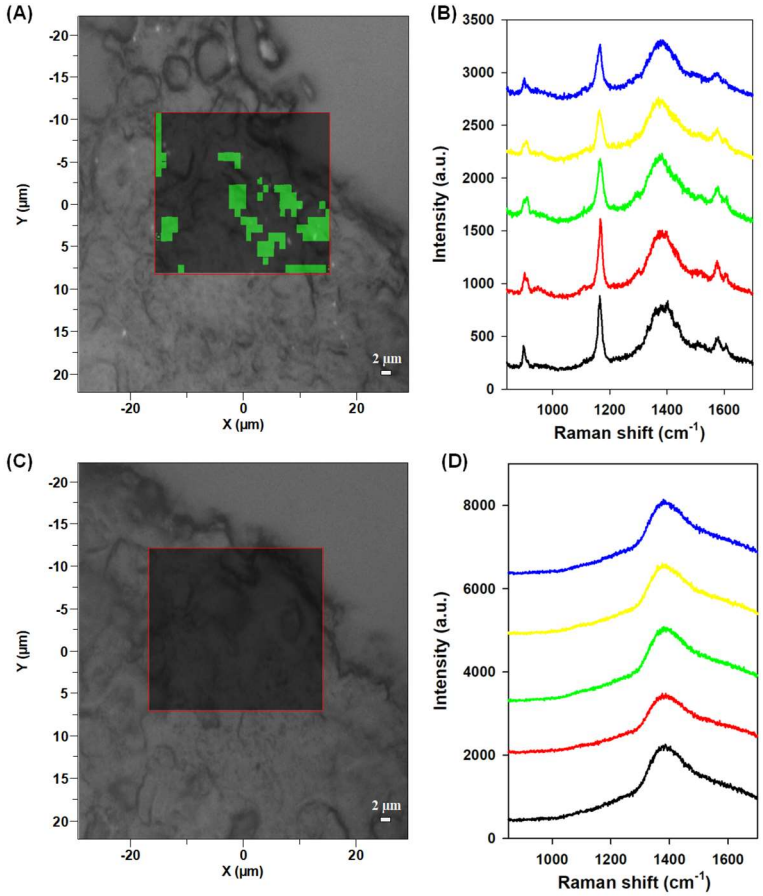

Figure 6. (A) Overlay of the optical image (100x magnification) and of the SERS map obtained on the ovarian cancerous tissue after incubation with the HS-PEG-FA-quenched nano-aggregates. (B) Representative spectra obtained in the pixels highlighted in green in the SERS intensity map of panel (A). (C) Overlay of the optical image (100x magnification) and of the SERS intensity map obtained on the ovarian cancerous tissue after incubation with the classical, non-aggregated Au nanotags functionalized with HS-PEG-FA. Mapping for this sample was performed with 85 mW of laser power at the sample (8.5 mW in panel A). (D) Representative spectra obtained at five different locations in the SERS intensity map of panel (C). Scale bar is 2 µm.

Both tissue sections were mapped by Raman microscopy using a 785 nm laser (8.5 mW power, 1 s acquisition time) and a spatial resolution of 1 µm in x-y directions. The MGITC Raman signal at 1170 cm^{-1} was used as the spectral marker to assess signal presence. For each pixel, the intensity at this wavenumber was compared to a threshold (see material and methods) allowing a binary classification of pixels as "signal-positive" or "signal-negative". When comparing adjacent tissue sections incubated either with the functionalized nano-aggregates or with functionalized classical Au nanoparticles (Figure 6A and 6C, respectively), numerous signal-positive pixels were observed in the case of nano-aggregates, while no pixels were highlighted for the Au NPs. Even at increased laser power (85 mW), no MGITC signal could be detected from the Au NP-labeled section (Figure 6D). Since both types of probes carry folic acid moieties and are known to exhibit high affinity for folate receptors, which are overexpressed in the tumor tissue, the absence of signal in the case of Au NPs (Figure 6D) can be attributed to their insufficient SERS sensitivity under these excitation conditions. In contrast, the nano-aggregates provided strong, easily detectable signals with only 1 s acquisition at low laser power (Figure 6B), confirming their superior enhancement properties and making them suitable for rapid Raman mapping. Additional tumor regions on the same tissue section were mapped, and similar results were consistently observed for both types of probes (Figure S25 and S27). Mapping of healthy tissue regions revealed only a few isolated signal-positive pixels (Figure S26), suggesting minimal non-specific binding and confirming that the detection of the SERS signal correlates with folate receptor overexpression.

Conclusion

In this work, we have demonstrated the production of SERS-active gold nano-aggregates using a microfluidic platform that enables precise control over nanoparticle aggregation. By using MGITC as both aggregating agent and Raman reporter, and employing a continuous flow system composed of two concatenated microreactors with HS-PEG-based quenching, we produced tunable and stable nano-aggregates exhibiting strong SERS signals under NIR excitation. The use of continuous microfluidic conditions enabled fine modulation of the aggregation extent via residence time and reagent flow rates, and introduced a high level of reversibility and automation unattainable in batch. The produced nano-aggregates provided at least a two-order-of-magnitude enhancement of the SERS signal over non-aggregated nanoparticles. Production of aggregates with other Raman reporter molecules (Crystal Violet and Rhodamine B isothiocyanate) was also demonstrated, highlighting the versatility of our approach. Furthermore, quenching of the aggregation with HS-PEG-Folic Acid allowed the direct production of targeting SERS nanotags with high specificity toward folate membrane receptor, often overexpressed in cancer tissues. These nano-aggregates yielded strong SERS contrast in tissue imaging experiments. Overall, our work provides a strong proof-of-concept highlighting the potential of microfluidic approaches to engineer advanced SERS-active plasmonic nanostructures with high performance and biological functionality. Nevertheless, further work is needed to fully explore the

possibilities offered by microfluidics to further improve the control of the aggregation process, with the goal of pushing the system toward a more homogeneous population of similarly-sized aggregates. Size fractionation of the aggregates could also be implemented to further select a defined range of aggregates size with optimal SERS enhancement. Also, the effect of other dyes or other NPs surface functions will be investigated to further understand their influence on the type of aggregates formed. Another interesting perspective could be to integrate inline purification of the aggregates to remove the PEG excess, yielding directly usable SERS nanotags for sustaining continuous delivery for biomedicine applications.

Supporting Information

Additional experimental details including photographs of experimental setup, additional data supporting the results presented in the manuscript.

Acknowledgements

Authors are grateful to Valérie Collard and Gilles Spronck for obtaining the SEM images. Authors acknowledge the CHU Biobank for providing the ovarian tissue sections (Ethical committee reference 2017/236). Alexandre Verdin and Pierre Stiernet acknowledge the Fonds de la Recherche Scientifique – FNRS for funding (postdoctoral fellowship).

References

(1) Gong, T.; Das, C. M.; Yin, M.-J.; Lv, T.-R.; Singh, N. M.; Soehartono, A. M.; Singh, G.; An, Q.-F.; Yong, K.-T. Development of SERS Tags for Human Diseases Screening and Detection. *Coord. Chem. Rev.* **2022**, *470*, 214711. https://doi.org/10.1016/j.ccr.2022.214711.

(2) Liu, H.; Gao, X.; Xu, C.; Liu, D. SERS Tags for Biomedical Detection and Bioimaging. *Theranostics* **2022**, *12* (4), 1870–1903. https://doi.org/10.7150/thno.66859.

(3) Lane, L. A.; Xue, R.; Nie, S. Emergence of Two Near-Infrared Windows for in Vivo and Intraoperative SERS. *Curr. Opin. Chem. Biol.* **2018**, *45*, 95–103. https://doi.org/10.1016/j.cbpa.2018.03.015.

(4) Deng, B.; Zhang, Y.; Qiu, G.; Li, J.; Lin, L. L.; Ye, J. NIR-II Surface-Enhanced Raman Scattering Nanoprobes in Biomedicine: Current Impact and Future Directions. *Small* **2024**, *20* (40), 2402235. https://doi.org/10.1002/smll.202402235.

(5) Pilot, R.; Massari, M. Silver Nanoparticle Aggregates: Wavelength Dependence of Their SERS Properties in the First Transparency Window of Biological Tissues. *Chem. Phys. Impact* **2021**, *2*, 100014. https://doi.org/10.1016/j.chphi.2021.100014.

(6) Bock, S.; Choi, Y.-S.; Kim, M.; Yun, Y.; Pham, X.-H.; Kim, J.; Seong, B.; Kim, W.; Jo, A.; Ham, K.-M.; Lee, S. G.; Lee, S. H.; Kang, H.; Choi, H. S.; Jeong, D. H.; Chang, H.; Kim, D.-E.; Jun, B.-H. Highly Sensitive Near-Infrared SERS Nanoprobes for in Vivo Imaging Using Gold-Assembled Silica Nanoparticles with Controllable Nanogaps. *J. Nanobiotechnology* **2022**, *20* (1), 130. https://doi.org/10.1186/s12951-022-01327-7.

(7) Kang, H.; Jeong, S.; Park, Y.; Yim, J.; Jun, B.-H.; Kyeong, S.; Yang, J.-K.; Kim, G.; Hong, S.; Lee, L. P.; Kim, J.-H.; Lee, H.-Y.; Jeong, D. H.; Lee, Y.-S. Near-Infrared SERS Nanoprobes with Plasmonic Au/Ag Hollow-Shell Assemblies for In Vivo Multiplex Detection. *Adv. Funct. Mater.* **2013**, *23* (30), 3719–3727. https://doi.org/https://doi.org/10.1002/adfm.201203726.

(8) Lee, S.; Dang, H.; Moon, J.-I.; Kim, K.; Joung, Y.; Park, S.; Yu, Q.; Chen, J.; Lu, M.; Chen, L.; Joo, S.-W.; Choo, J. SERS-Based Microdevices for Use as in Vitro Diagnostic Biosensors. *Chem. Soc. Rev.* **2024**, *53* (11), 5394–5427. https://doi.org/10.1039/D3CS01055D.

(9) Verdin, A.; Malherbe, C.; Eppe, G. Designing SERS Nanotags for Profiling Overexpressed Surface Markers on Single Cancer Cells: A Review. *Talanta* **2024**, *276*, 126225. https://doi.org/10.1016/j.talanta.2024.126225.

(10) Becerril-Castro, I. B.; Calderon, I.; Pazos-Perez, N.; Guerrini, L.; Schulz, F.; Feliu, N.; Chakraborty, I.; Giannini, V.; Parak, W. J.; Alvarez-Puebla, R. A. Gold Nanostars: Synthesis, Optical and SERS Analytical Properties. *Anal. Sens.* **2022**, *2* (3), e202200005. https://doi.org/10.1002/anse.202200005.

(11) Andreiuk, B.; Nicolson, F.; Clark, L. M.; Panikkanvalappil, S. R.; Kenry; Rashidian, M.; Harmsen, S.; Kircher, M. F. Design and Synthesis of Gold Nanostars-Based SERS Nanotags for Bioimaging Applications. *Nanotheranostics* **2022**, *6* (1), 10–30. https://doi.org/10.7150/ntno.61244.

(12) He, H.; Zhang, Y.; Zhu, S.; Ye, J.; Lin, L. Resonant Strategy in Designing NIR-II SERS Nanotags: A Quantitative Study. *J. Phys. Chem. C* **2022**, *126* (30), 12575–12581. https://doi.org/10.1021/acs.jpcc.2c02512.

(13) Atta, S.; Tsoulos, T. V; Fabris, L. Shaping Gold Nanostar Electric Fields for Surface-Enhanced Raman Spectroscopy Enhancement via Silica Coating and Selective Etching. *J. Phys. Chem. C* **2016**, *120* (37), 20749–20758. https://doi.org/10.1021/acs.jpcc.6b01949.

(14) Khatua, S.; Paulo, P. M. R.; Yuan, H.; Gupta, A.; Zijlstra, P.; Orrit, M. Resonant Plasmonic Enhancement of Single-Molecule Fluorescence by Individual Gold Nanorods. *ACS Nano* **2014**, *8* (5), 4440–4449. https://doi.org/10.1021/nn406434y.

(15) Siegel, A. L.; Baker, G. A. Bespoke Nanostars: Synthetic Strategies, Tactics, and Uses of Tailored Branched Gold Nanoparticles. *Nanoscale Adv.* **2021**, *3* (14), 3980–4004. https://doi.org/10.1039/D0NA01057J.

(16) Rodríguez-Lorenzo, L.; Romo-Herrera, J. M.; Pérez-Juste, J.; Alvarez-Puebla, R. A.; Liz-Marzán, L. M. Reshaping and LSPR Tuning of Au Nanostars in the Presence of CTAB. *J. Mater. Chem.* **2011**, *21* (31), 11544–11549. https://doi.org/10.1039/C1JM10603A.

(17) Höller, R. P. M.; Jahn, I. J.; Cialla-May, D.; Chanana, M.; Popp, J.; Fery, A.; Kuttner, C. Biomacromolecular-Assembled Nanoclusters: Key Aspects for Robust Colloidal SERS Sensing. *ACS Appl. Mater. Interfaces* **2020**, *12* (51), 57302–57313. https://doi.org/10.1021/acsami.0c16398.

(18) Tan, X.; Wang, Z.; Yang, J.; Song, C.; Zhang, R.; Cui, Y. Polyvinylpyrrolidone-(PVP-) Coated Silver Aggregates for High Performance Surface-Enhanced Raman Scattering in Living Cells. *Nanotechnology* **2009**, *20* (44), 445102. https://doi.org/10.1088/0957-4484/20/44/445102.

(19) Leng, W.; Vikesland, P. J. MGITC Facilitated Formation of AuNP Multimers. *Langmuir* **2014**, *30* (28), 8342–8349. https://doi.org/10.1021/la501807n.

(20) Yoon, S. Controlled Assembly of Gold Nanoparticles: Methods and Plasmon Coupling Properties. *Bull. Korean Chem. Soc.* **2024**, *45* (8), 689–698. https://doi.org/10.1002/bkcs.12886.

(21) Blakey, I.; Merican, Z.; Thurecht, K. J. A Method for Controlling the Aggregation of Gold Nanoparticles: Tuning of Optical and Spectroscopic Properties. *Langmuir* **2013**, *29* (26), 8266–8274. https://doi.org/10.1021/la401361u.

(22) Yan, S.; Zhang, Z.; Chen, J.; Wang, Q.; Wu, Y.; Sui, Y.; Wang, S.; Che, Q.; Zhou, N.; Chen, L.; Chen, L. Cavity-Like Silver Aggregates-Based Colloidal SERS Microfluidic Platform for Highly Reproducible Online Reaction Process Analysis. *Small* **2025**, *21* (30), 2501338. https://doi.org/10.1002/smll.202501338.

(23) Zhang, W. Nanoparticle Aggregation: Principles and Modeling; Capco, D. G., Chen, Y., Eds.; Springer Netherlands: Dordrecht, 2014; pp 19–43. https://doi.org/10.1007/978-94-017-8739-0_2.

(24) Sloan-Dennison, S.; Wallace, G. Q.; Hassanain, W. A.; Laing, S.; Faulds, K.; Graham, D. Advancing SERS as a Quantitative Technique: Challenges, Considerations, and Correlative Approaches to Aid Validation. *Nano Converg.* **2024**, *11* (1), 33. https://doi.org/10.1186/s40580-024-00443-4.

(25) Freitag, I.; Neugebauer, U.; Csaki, A.; Fritzsche, W.; Krafft, C.; Popp, J. Preparation and Characterization of Multicore SERS Labels by Controlled Aggregation of Gold Nanoparticles. *Vib. Spectrosc.* **2012**, *60*, 79–84. https://doi.org/10.1016/j.vibspec.2012.02.013.

(26) Skinner, W. H.; Sala, R. L.; Sokolowski, K.; Blein-Dezayes, I.; Potter, N. S.; Mosca, S.; Gardner, B.; Baumberg, J. J.; Matousek, P.; Scherman, O. A.; Stone, N. An All-in-One Nanoheater and Optical Thermometer Fabricated from Fractal Nanoparticle Assemblies. *ACS Nano* **2025**, *19* (14), 13779–13789. https://doi.org/10.1021/acsnano.4c16452.

(27) Potter, N. S.; Sokołowski, K.; Sala, R. L.; McCune, J. A.; Scherman, O. A. Kinetically Arrested SERS-Active Aggregates for Biosensing. *Chem. – A Eur. J.* **2025**, *n/a* (n/a), e202500915. https://doi.org/10.1002/chem.202500915.

(28) Wei, H.; Willner, M. R.; Marr, L. C.; Vikesland, P. J. Highly Stable SERS PH Nanoprobes Produced by Co-Solvent Controlled AuNP Aggregation. *Analyst* **2016**, *141* (17), 5159–5169. https://doi.org/10.1039/C6AN00650G.

(29) Peng, X.; Zhang, M.; Xue, F.; Zhang, A.; Xu, Y.; Huang, Y.; Wang, H.; Chen, H. A General Method for Precise Chain Assembly of Noble Metal Nanoparticles. *Mater. Chem. Front.* **2023**, *7* (15), 3073–3081. https://doi.org/10.1039/D3QM00229B.

(30) Cheng, J.; Zhang, Z.; Zhang, L.; Miao, J.; Chen, Y.; Zhao, R.; Liu, M.; Chen, L.; Wang, X. Size-Controllable Colloidal Ag Nano-Aggregates with Long-Time SERS Detection Window for on-Line High-Throughput Detection. *Talanta* **2023**, *257*, 124358. https://doi.org/10.1016/j.talanta.2023.124358.

(31) Yan, S.; Chen, L.; Zhang, Z. Utilizing Freeze-Thaw-Ultrasonication to Prepare Mesoporous Silica-Encapsulated Colloidal Silver Nanoaggregates with Long-Term Surface-Enhanced Raman Spectroscopy Activity. *Sensors* **2025**, *25* (6), 1840. https://doi.org/10.3390/s25061840.

(32) Zhou, T.; Zhang, Z. Centrifugation-Induced Stable Colloidal Silver Nanoparticle Aggregates for Reproducible Surface-Enhanced Raman Scattering Detection. *Biosensors*. 2025. https://doi.org/10.3390/bios15050298.

(33) Huang, P.-J.; Chau, L.-K.; Yang, T.-S.; Tay, L.-L.; Lin, T.-T. Nanoaggregate-Embedded Beads as Novel Raman Labels for Biodetection. *Adv. Funct. Mater.* **2009**, *19* (2), 242–248. https://doi.org/10.1002/adfm.200800961.

(34) Ding, S.-Y.; Yi, J.; Li, J.-F.; Ren, B.; Wu, D.-Y.; Panneerselvam, R.; Tian, Z.-Q. Nanostructure-Based Plasmon-Enhanced Raman Spectroscopy for Surface Analysis of Materials. *Nat. Rev. Mater.* **2016**, *1* (6), 16021. https://doi.org/10.1038/natrevmats.2016.21.

(35) Abou-Hassan, A.; Sandre, O.; Cabuil, V. Microfluidics in Inorganic Chemistry. *Angew. Chemie Int. Ed.* **2010**, *49* (36), 6268–6286. https://doi.org/10.1002/anie.200904285.

(36) Darby, B. L.; Le Ru, E. C. Competition between Molecular Adsorption and Diffusion: Dramatic Consequences for SERS in Colloidal Solutions. *J. Am. Chem. Soc.* **2014**, *136* (31), 10965–10973. https://doi.org/10.1021/ja506361d.

(37) Liu, Y.; Jiang, X. Why Microfluidics? Merits and Trends in Chemical Synthesis. *Lab Chip* **2017**, *17* (23), 3960–3978. https://doi.org/10.1039/C7LC00627F.

(38) Voisin, F.; Lelong, G.; Guigner, J.-M.; Bizien, T.; Mallet, J.-M.; Carn, F. Flash Colloidal Gold Nanoparticle Assembly in a Milli Flow System: Implications for Thermoplasmonic and for the Amplification of Optical Signals. *ACS Appl. Nano Mater.* **2022**, *5* (5), 6964–6971. https://doi.org/10.1021/acsanm.2c00944.

(39) Scaranti, M.; Cojocaru, E.; Banerjee, S.; Banerji, U. Exploiting the Folate Receptor α in Oncology. *Nat. Rev. Clin. Oncol.* **2020**, *17* (6), 349–359. https://doi.org/10.1038/s41571-020-0339-5.

(40) Xue, Y.; Li, X.; Li, H.; Zhang, W. Quantifying Thiol-Gold Interactions towards the Efficient Strength Control. *Nat. Commun.* **2014**, *5* (1), 4348. https://doi.org/10.1038/ncomms5348.

(41) Cheng, H.-W.; Lim, S. I.; Fang, W.; Yan, H.; Skeete, Z.; Ngo, Q. M.; Luo, J.; Zhong, C.-J. Assessing Interparticle J-Aggregation of Two Different Cyanine Dyes with Gold Nanoparticles and Their Spectroscopic Characteristics. *J. Phys. Chem. C* **2015**, *119* (49), 27786–27796. https://doi.org/10.1021/acs.jpcc.5b09973.

(42) Lim, I.-I. S.; Maye, M. M.; Luo, J.; Zhong, C.-J. Kinetic and Thermodynamic Assessments of the Mediator−Template Assembly of Nanoparticles. *J. Phys. Chem. B* **2005**, *109* (7), 2578–2583. https://doi.org/10.1021/jp045702f.

(43) Nepal, D.; Park, K.; Vaia, R. A. High-Yield Assembly of Soluble and Stable Gold Nanorod Pairs for High-Temperature Plasmonics. *Small* **2012**, *8* (7), 1013–1020. https://doi.org/10.1002/smll.201102152.

(44) Nabika, H.; Oikawa, T.; Iwasaki, K.; Murakoshi, K.; Unoura, K. Dynamics of Gold Nanoparticle Assembly and Disassembly Induced by PH Oscillations. *J. Phys. Chem. C* **2012**, *116* (10), 6153–6158. https://doi.org/10.1021/jp300650c.

(45) de Oliveira, T. A.; Setti, G. O.; Rubira, R. J. G.; Constantino, C. J. L. Tailoring Aggregation of Silver Nanoparticles via Crystal Violet: A Surface-Enhanced Raman Scattering Perspective. *Colloids Surfaces A Physicochem. Eng. Asp.* **2025**, *724*, 137477. https://doi.org/10.1016/j.colsurfa.2025.137477.

(46) Vu, N. N.; Ng, K. W.; Jaitpal, S.; Negahdary, M.; Nguyen, T.; Kodam, R. S.; Mabbott, S. High Precision Automated Synthesis of Surface-Enhanced (Resonance) Raman Nanotags. *ACS Sensors* **2025**. https://doi.org/10.1021/acssensors.5c00068.

(47) Chegel, V.; Rachkov, O.; Lopatynskyi, A.; Ishihara, S.; Yanchuk, I.; Nemoto, Y.; Hill, J. P.; Ariga, K. Gold Nanoparticles Aggregation: Drastic Effect of Cooperative Functionalities in a Single Molecular Conjugate. *J. Phys. Chem. C* **2012**, *116* (4), 2683–2690. https://doi.org/10.1021/jp209251y.

(48) Shi, L.; Zhang, J.; Zhao, M.; Tang, S.; Cheng, X.; Zhang, W.; Li, W.; Liu, X.; Peng, H.; Wang, Q. Effects of Polyethylene Glycol on the Surface of Nanoparticles for Targeted Drug Delivery. *Nanoscale* **2021**, *13* (24), 10748–10764. https://doi.org/10.1039/D1NR02065J.

(49) Arenas-Guerrero, P.; Delgado, Á. V; Donovan, K. J.; Scott, K.; Bellini, T.; Mantegazza, F.; Jiménez, M. L. Determination of the Size Distribution of Non-Spherical Nanoparticles by Electric Birefringence-Based Methods. *Sci. Rep.* **2018**, *8* (1), 9502.

https://doi.org/10.1038/s41598-018-27840-0.

(50) Freeman, R. G.; Bright, R. M.; Hommer, M. B.; Natan, M. J. Size Selection of Colloidal Gold Aggregates by Filtration: Effect on Surface-Enhanced Raman Scattering Intensities. *J. Raman Spectrosc.* **1999**, *30* (8), 733–738. https://doi.org/10.1002/(SICI)1097-4555(199908)30:8<733::AID-JRS433>3.0.CO;2-E.

(51) Khlebtsov, N. G.; Khlebtsov, B. N.; Kryuchkova, E. V; Zarkov, S. V; Burov, A. M. Universal Determination of Gold Concentration in Colloids with UV–Vis Spectroscopy. *J. Phys. Chem. C* **2022**, *126* (45), 19268–19276. https://doi.org/10.1021/acs.jpcc.2c05843.

(52) Verdin, A.; Sloan-Dennison, S.; Malherbe, C.; Graham, D.; Eppe, G. SERS Nanotags for Folate Receptor α Detection at the Single Cell Level: Discrimination of Overexpressing Cells and Potential for Live Cell Applications. *Analyst* **2022**, *147* (14), 3328–3339. https://doi.org/10.1039/d2an00706a.

(53) Verdin, A.; Malherbe, C.; Müller, W. H.; Bertrand, V.; Eppe, G. Multiplex Micro-SERS Imaging of Cancer-Related Markers in Cells and Tissues Using Poly(Allylamine)-Coated Au@Ag Nanoprobes. *Anal. Bioanal. Chem.* **2020**, *412* (28), 7739–7755. https://doi.org/10.1007/s00216-020-02927-8.

Graphical Abstract